Next-level high-precision spatial omics enabled through spatial similarity networking

Varun V. Sharma[1]*, Gabor Toth[1,2]*, Robert Martinis[1], Cathrin E. Hansen[3,4,5], Gijs Kooij[3,4,5,6], Ingela Lanekoff[1,2#]

[1] Department of Chemistry - BMC, Uppsala University, Uppsala, Sweden
[2] Center of Excellence for the Chemical Mechanisms of Life, Uppsala University, Sweden
[3] Amsterdam UMC, Location VU Medical Center, Department of Molecular Cell Biology and Immunology, De Boelelaan 1117, Amsterdam, The Netherlands
[4] Amsterdam Neuroscience, Amsterdam UMC, Amsterdam, The Netherlands
[5] MS Center Amsterdam, Amsterdam UMC, Location VU Medical Center, Amsterdam, The Netherlands
[6] Amsterdam Institute for Immunology and Infectious Diseases, Amsterdam UMC, Amsterdam, The Netherlands

* Both authors contributed equally to this work
[#] Corresponding author

Unambiguous molecular annotations are essential to discern complex local biochemical processes in spatial biology. Here, we acquire conventional mass spectrometry images (MSI) in parallel with hundreds of tandem MSI and introduce spatial similarity networks as an additional dimension for molecular annotation. Overall, our approach enables the deconvolution and annotation of superimposed and otherwise unresolvable molecular images, advancing spatial omics to the frontier of comprehensive omics technologies.

Mass spectrometry imaging (MSI) enables highly multiplexed label-free visualization of molecular distributions in biological tissues and is central to spatial omics research.[1] While high mass resolving power and ion mobility spectrometry enhance molecular specificity,[2] tandem mass spectrometry (MS^2) is crucial for differentiating isomers and unresolved isobars.[3,4] Consequently, MS^2 imaging (MS^2I) can reveal both molecular structure and spatial distribution.[5] Despite its potential, MS^2I remains rare due to challenges in maintaining sensitivity, spatial resolution, throughput and scalability, and consistent precursor selection. Existing state-of-the-art MS^2 approaches, including data-dependent acquisition (DDA),[6] dataset-dependent acquisition,[7] and conventional targeted MS^2 imaging,[8] fall short of overcoming these barriers. Here, we utilize Parallel Image Acquisition (PIA), which integrates the instrument's parallel MS^2 capabilities with MSI, thereby overcoming previous technical challenges for MS^2I. To interpret complex PIA data, we developed the Spatial Similarity Network (SSN) software, adding a new dimension to image-based annotation via product ion spatial networks. This ultimately facilitates large-scale high-precision spatial omics with MS^2I.

Data were obtained by PIA using a tribrid mass spectrometer comprising a quadrupole, an Orbitrap (FT), and an ion trap (IT) mass analyzer, coupled with pneumatically assisted nanospray desorption electrospray ionization (PA nano-DESI).[9] Specifically, during one high-mass-resolution scan in the FT ($m/\Delta m$ = 500,000 at *m/z* 200), the IT simultaneously acquires MS^2 spectra in a targeted approach, all within one pixel (Fig. 1). The number of fragmentation windows can be expanded by cycling multiple inclusion lists (e.g. N = 4 in Fig 1a). Thus, thousands of MS^2 ion images are generated from a single experiment (Fig. 1a–e). To process this vast amount of complex data generated by PIA, we developed the SSN software tool and integrated it into our ion-to-image (i2i) software (Extended Data Fig. 1).[10] The SSN computes and clusters ions based on their spatial distributions, visualizing them as a network where each node represents an ion (Fig. 1g, Extended Data Figs. 2,3 and Supplementary Figs. 1,2). Ions with similar distributions cluster together, and a cluster containing various product ions indicates that these originate from the same precursor. The molecular structure of the precursor can be automatically assigned by uploading a product ion library into the software (Supplementary Fig. 3 and Table 1-3). Therefore, the SSN deciphers complex data, identifies product ions originating from the same precursor, and enables automatic annotation, which can be cross-referenced with accurate mass-derived precursor ion annotations (Fig. 1h-i). Overall, SSN utilizes product ion images as the third orthogonal dimension, alongside accurate mass measurements and fragmentation spectra, for the unambiguous annotation of otherwise non-resolvable molecules.

We demonstrate the capabilities of our approach by imaging mouse brain tissue with PIA using four inclusion lists, yielding a total of 108 (27×4) fragmentation windows (±0.35) in ~7,500 out of ~35,000 pixels (Fig. 1 and Extended Data Fig. 4, Supplementary Table 4). Following, SSN was used to deconvolute the molecular complexity of the vast dataset. For example, in 34 selected fragmentation windows, the spatial distribution and molecular structure of 134 isomers and isobars were resolved. Specifically, these include 70 phosphatidylcholines (PC), 44 phosphatidylethanolamines (PE), and 20 PE-plasmalogens, which were reproducibly detected in several datasets (Extended Data Fig. 5, Supplementary Fig. 4 and Tables 5,6). Strikingly, 75 of these molecules could not be resolved by MSI despite a high mass resolving power ($m/\Delta m$ = 500,000 at *m/z* 200). In conclusion, the combination of PIA and SSN uniquely identifies and distinguishes superimposed isobaric and isomeric spatial distributions, providing a solid foundation for biological interpretations.

To provide proof of principle in a human setting, we applied our approach to human brain tissue from subjects with multiple sclerosis. Here, our platform proved instrumental in detecting low-abundant and poorly ionizable molecules, underscoring its utility for high-precision spatial omics of complex pathological samples. With demyelination being a major pathological hallmark of multiple sclerosis,[11] it is particularly interesting to reveal local cholesterol levels,[12] which is a key constituent of neuronal myelin sheets.[13] Additionally, it is intriguing to study the chemical profiles surrounding the blood-brain barrier (BBB), which can provide valuable insights into BBB leakage that is another pathological hallmark of the disease.[14] We successfully mapped the distribution of cholesterol and six oxysterols in white matter tissue (Fig. 2 and Supplementary Fig. 5-7). Despite the high complexity of the mass spectra, the SSN software efficiently clustered and automatically annotated the sterols (Fig. 2a-d, Extended Data Fig. 6 and Supplementary Fig 8, Table 7).[15] Importantly, cholestanetetraol (ST6) and 24-homodeoxycholic acid (ST7) were found to localize to a BBB leakage site (Fig. 2e). Since these sterols are not biosynthesized in the brain, these images support the occurrence of BBB disruption in multiple sclerosis pathology.[16]

To correlate the abundance of sterols with the severity of demyelination in the detected lesion areas, we determined the stage of demyelination using proteolipid protein (PLP) expression in tissues from three non-neurological controls and five individuals with multiple sclerosis (PwMS) (Extended Data Fig. 7). This revealed a 2-fold depletion of cholesterol and an ~2-fold increase of ST4 and ST7 in regions exhibiting diffuse and absent myelin compared to areas with normal myelin (Fig. 2f-g). Additionally, an increasing trend was observed for ST3, which has been previously reported to be neurotoxic.[17] These results suggest that cholesterol undergoes oxidization during the demyelination process in affected brain regions. Furthermore, our results indicate an overall heightened cholesterol oxidation in brain tissues from PwMS, (Fig. 2g and Extended Data Fig 8). Thus, with our approach, we highlight the potential role of local cholesterol oxidation in multiple sclerosis lesions and show that it warrants further investigations.

In summary, our combined approach with PIA and SSN provides a powerful new platform for high-precision spatial omics. This facilitates both extensive molecular coverage from MS^2I and detailed molecular structure analysis based on spatial distribution, with the SSN seamlessly integrated into our i2i software. In particular, we show the distribution and detailed molecular structure characterization of isomeric and isobaric phospholipids in addition to the much less abundant oxysterols. In the context of multiple sclerosis, we observed strong indications of increased BBB leakage and the implication of cholesterol oxidation in demyelinated lesion areas. While our applications primarily highlight metabolomics, the strategy is versatile and applicable to proteomics, glycomics and pharmacokinetics. Moreover, coupling PIA and SSN with higher spatial or tandem mass resolution instrumentation,[18] or reactive chemistry workflows,[19,20] could further deepen structural characterization. Ultimately, PIA and SSN pioneer the integration of large-scale information-rich molecular distributions with enhanced structural characterization, setting a new benchmark in spatial omics.

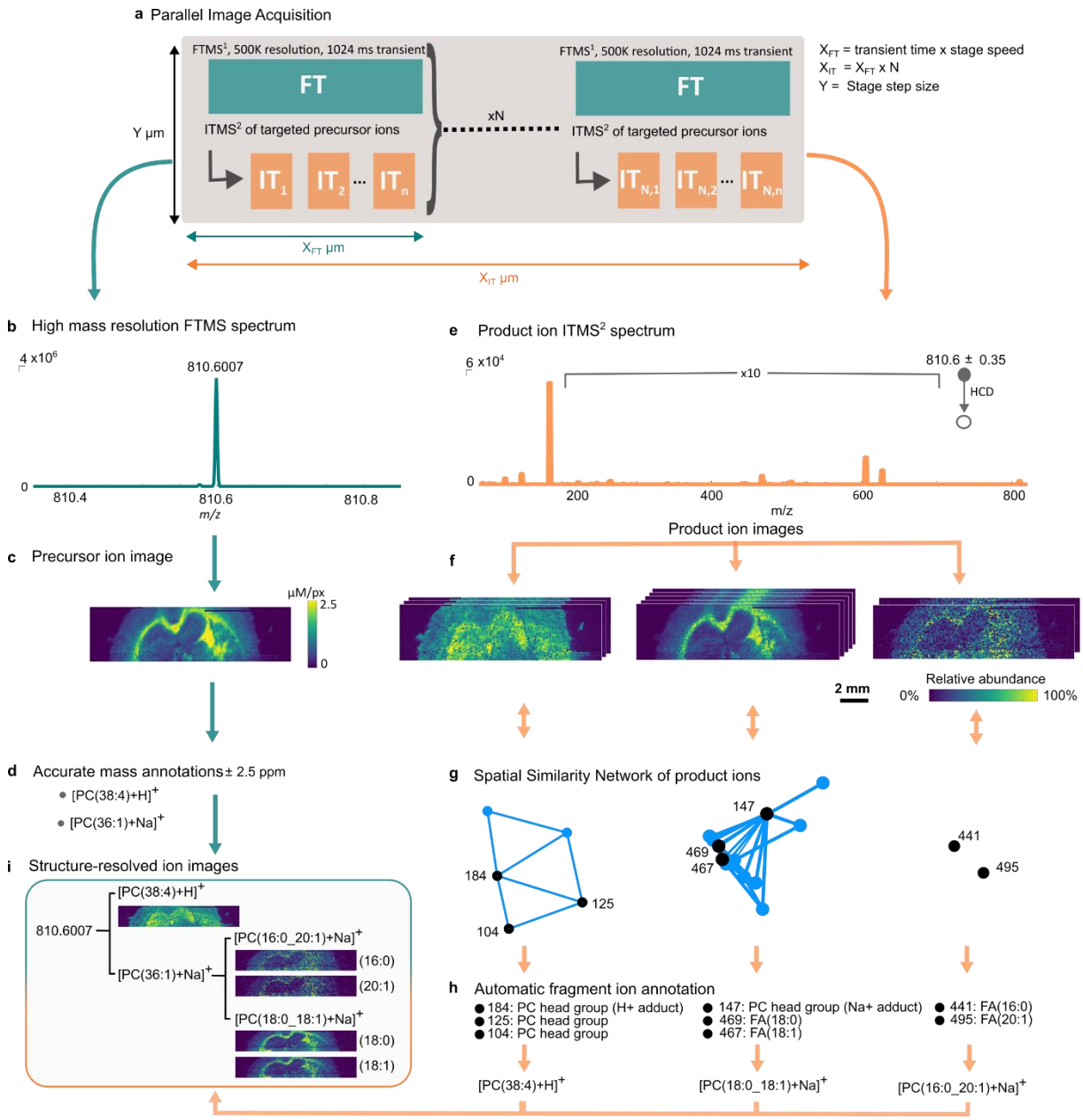

Fig 1 | Workflow of PIA SSN. a, Schematic of PIA where one full FTMS scan with n serial ITMS^2 scans are acquired in each pixel. Additional precursors are included by looping N number of inclusion lists. **b,c,d,** The acquired FTMS spectrum from mouse brain tissue has high mass resolution **(b),** quantitative MS^{1}I is achieved through normalization to internal standards in the PA nano-DESI solvent **(c),** and putative annotation of the precursor is enabled by accurate mass **(d)**. In the example FTMS spectrum **(b),** putative annotation *m/z* 810.6007 suggests [PC(38:4)+H]$^+$ and [PC(36:1)+Na]$^+$. **e,f,g,h,** All product ions from all precursors in the isolation window are detected in the ITMS^2 spectra **(e)** and each have their unique product ion image **(f)**. Product ion in this example **(e)**, were grouped based on their spatial similarity score **(g)**, calculated by the SSN addition to our i2i software. Product ions are annotated through our in-house compiled library **(h)** that in combination with the accurate mass annotation enables full structural annotation of *m/z* 810.6007 revealing an **(i)** isobaric mixture of [PC(38:4)+H]$^+$ and [PC(36:1)+Na]$^+$ and an isomeric mixture of [PC(18:0_18:1)+Na]$^+$ and [PC(16:0_20:1)+Na]$^+$. HCD, higher energy collision-induced dissociation. N=4 and n=27.

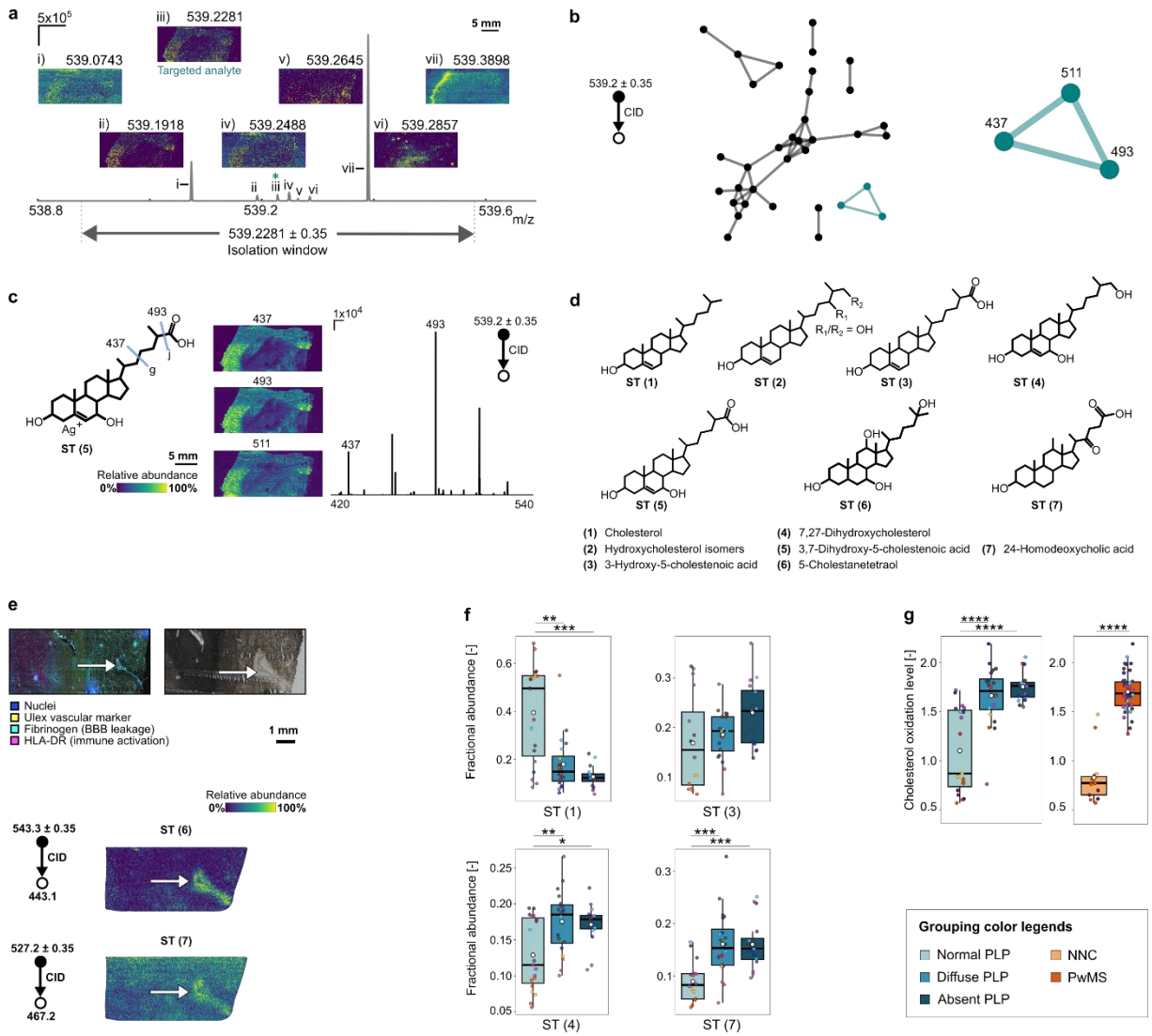

Fig 2 | Cholesterol oxidation products detected in human multiple sclerosis brain tissues. a,b,c,d, Structural annotation of cholesterol and oxysterols $[M+^{107}Ag]^+$. An FTMS spectrum detailing the isolation window of ions selected for $ITMS^2$ **(a)** with the corresponding SSN clusters **(b)** and an example (*m/z* 539.2) with product ion images and fragmentation sites from one cluster **(c)**. Structure of cholesterol and identified oxysterol species from tissue **(d)**. **e,f,g,** Multimodal study revealing altered cholesterol and oxysterol profiles in demyelinated areas. Representative image of UEA-I, Fibrinogen and HLA-DR immunoreactivity and optical image with corresponding images of diagnostic product ions for cholestanetetraol (ST 6) and 24-homodeoxycholic acid (ST 7), white arrow: BBB leakage site **(e)**. Boxplots represent the fractional abundance of significantly decreased cholesterol (ST 1) and increased oxysterol (ST 3, ST 4, ST 7) species **(f)**. Point colors indicate individual donors as per Supplementary Table 8, black line denotes the median and the white point the mean **(g)**. Level of oxysterol oxidation significantly increases in diffuse and absent PLP category compared to normal PLP and is higher in PwMS compared to NNCs. For calculations see Methods section. PLP, proteolipidprotein staining of myelin; HLA-DR, Human Leukocyte Antigen – DR isotype; BBB, blood brain barrier; Ulex: Ulex Europaeus Agglutinin I (UEA I), non-neurological control (NNC), people with multiple sclerosis (PwMS). (*:p<0.05, **:p<0.01, ***:p<0.001, ****:p<0.0001).

References

1. Doerr, A. Mass spectrometry imaging takes off. *Nat Methods* **15**, 32–32 (2018).

2. Xu, S. *et al.* Spatially and temporally probing distinctive glycerophospholipid alterations in Alzheimer's disease mouse brain via high-resolution ion mobility-enabled sn-position resolved lipidomics. *Nat Commun* **15**, 6252 (2024).

3. Weigand, M. R. *et al.* Lipid Isobar and Isomer Imaging Using Nanospray Desorption Electrospray Ionization Combined with Triple Quadrupole Mass Spectrometry. *Anal Chem* (2024) doi:10.1021/acs.analchem.3c04705.

4. Skotland, T. *et al.* Pitfalls in lipid mass spectrometry of mammalian samples — a brief guide for biologists. *Nat Rev Mol Cell Biol* **25**, 759–760 (2024).

5. Guo, X. *et al.* Tandem Mass Spectrometry Imaging Enables High Definition for Mapping Lipids in Tissues. *Angewandte Chemie - International Edition* **62**, (2023).

6. Ellis, S. R. *et al.* Automated, parallel mass spectrometry imaging and structural identification of lipids. *Nat Methods* **15**, 515–518 (2018).

7. Heuckeroth, S. *et al.* On-tissue dataset-dependent MALDI-TIMS-MS2 bioimaging. *Nat Commun* **14**, 7495 (2023).

8. Lanekoff, I. *et al.* High-speed tandem mass spectrometric in situ imaging by nanospray desorption electrospray ionization mass spectrometry. *Anal Chem* **85**, 9596–9603 (2013).

9. Duncan, K. D., Bergman, H. M. & Lanekoff, I. A pneumatically assisted nanospray desorption electrospray ionization source for increased solvent versatility and enhanced metabolite detection from tissue. *Analyst* **142**, 3424–3431 (2017).

10. Lillja, J., Duncan, K. D. & Lanekoff, I. Ion-to-Image, i2i, a Mass Spectrometry Imaging Data Analysis Platform for Continuous Ionization Techniques. *Anal Chem* **95**, 11589–11595 (2023).

11. Reich, D. S., Lucchinetti, C. F. & Calabresi, P. A. Multiple Sclerosis. *New England Journal of Medicine* **378**, 169–180 (2018).

12. Yutuc, E. *et al.* Localization of sterols and oxysterols in mouse brain reveals distinct spatial cholesterol metabolism. *Proceedings of the National Academy of Sciences* **117**, 5749–5760 (2020).

13. Cantuti-Castelvetri, L. *et al.* Defective cholesterol clearance limits remyelination in the aged central nervous system. *Science (1979)* **359**, 684–688 (2018).

14. Zierfuss, B., Larochelle, C. & Prat, A. Blood–brain barrier dysfunction in multiple sclerosis: causes, consequences, and potential effects of therapies. *Lancet Neurol* **23**, 95–109 (2024).

15. Sharma, V. V. & Lanekoff, I. Revealing Structure and Localization of Steroid Regioisomers through Predictive Fragmentation Patterns in Mass Spectrometry Imaging. *Anal Chem* (2023) doi:10.1021/acs.analchem.3c03931.

16. Hansen, C. E. *et al.* Inflammation-induced TRPV4 channels exacerbate blood–brain barrier dysfunction in multiple sclerosis. *J Neuroinflammation* **21**, 72 (2024).

17. Theofilopoulos, S. *et al.* Cholestenoic acids regulate motor neuron survival via liver X receptors. *Journal of Clinical Investigation* **124**, 4829–4842 (2014).

18. Kuster, B., Tüshaus, J. & Bayer, F. P. A new mass analyzer shakes up the proteomics field. *Nat Biotechnol* **42**, 1796–1797 (2024).

19. Paine, M. R. L. *et al.* Mass Spectrometry Imaging with Isomeric Resolution Enabled by Ozone-Induced Dissociation. *Angewandte Chemie International Edition* **57**, 10530–10534 (2018).

20. Ma, X. & Xia, Y. Pinpointing Double Bonds in Lipids by Paternò-Büchi Reactions and Mass Spectrometry. *Angewandte Chemie International Edition* **53**, 2592–2596 (2014).

Methods

Sample selection for model experiments

Mouse brain (8–10 weeks old male C57BL/6) was purchased from Creative Biolabs (Shirley, NY, USA) and cut to a thickness of 10 µm using a cryo-microtome (Leica Microsystems, Wetzlar, Germany). The sections were thaw-mounted onto regular microscope glass slides and stored at -80 °C prior to analysis.

Sample selection for analysis of human tissue samples

Freshly frozen post-mortem human brain samples were obtained from the Netherlands Brain Bank from 5 clinically diagnosed MS patients (mean age at death: 65 years) and 3 non-neurological controls (mean age at death: 66 years). Tissue blocks were cut into 10 µm sections and stored at -80 °C until further use. All donors or their next of kin provided fully informed consent for autopsy and use of material for research from the Netherlands Brain Bank under ethical approval by the Medical Ethics Committee of the Free University Medical Center in Amsterdam (2009/148), project number 1,127. Donor details are shown in Supplementary Table 8.

Parallel image acquisition using PA nano-DESI

Samples were gently thawed at room temperature under constant airflow before analysis. Mouse brain sections were analyzed without any sample preparation, human multiple sclerosis tissue sections were dipped six times in deionized water (Milli-Q, 18.2 MΩ) for one minute each to remove excess salts. For MSI, the samples were placed on an XYZ linear motor stage (Zaber Technologies Inc., Vancouver, BC), controlled via a custom-designed LABVIEW program.[21]

The PA nano-DESI was set up as previously described,[9] using 150/50 µm o.d./i.d. fused silica capillaries (Genetek, Sweden). Briefly, the primary capillary, connected to a syringe containing the nano-DESI solvent, was coupled to a pneumatically assisted secondary capillary positioned at ~90 degrees. The extraction solvent was delivered through the primary capillary via a syringe pump (Legato 180, KD Scientific, Holliston, USA), with the ESI voltage applied directly to the syringe needle. The probe and sample positioning were monitored using long-working-distance digital optical microscopes (Dino-Lite, USA).

Mass spectrometry was performed in positive ion mode on an Orbitrap IQ-X (Thermo Fisher Scientific, San Jose, CA, USA) using high-resolution Orbitrap (FTMS) MS^1 and ion trap (ITMS) MS^2 modes, or $FTMS^2$ for accurate mass confirmation. For PIA, ions were first selected for a full FTMS scan and subsequently for several parallel MS^2 scans in the ion trap during the FTMS transition time.[22] The PIA methodology was tested across five different experimental conditions (varying extraction solvents and targeted analytes) to demonstrate its versatility (Supplementary Table 6). Detailed PA nano-DESI and mass spectrometry acquisition parameters for each experiment are provided in Supplementary Table 9.

Figures showing data and metadata from the experiments were exported from FreeStyle 1.8 SP2, v1.8.63.0. Ion images were generated using our in-house software tool, i2i,[11] from .mzML data converted via MSConvertGUI (ProteoWizard, v3.0.22285) from .RAW files. The use of. mzML format facilitates a vendor-neutral use of the software. Ion images of the MS^2 data was created by imputing the scans on a master grid generated from the FTMS scans where the specific MS^2 spectra were given the same coordinates as the closest FTMS master scan.

Spatial similarity network analysis

The SSN is computed based on the intensities of all identified *m/z* values in all pixels. First, the user selects the scan filter, scan type, and search parameters. Although the GUI provides suggested pre-set parameters for ppm tolerance and min and max intensities, these may need to be altered based on the experiment. Secondly, the user selects if the SSN should be computed using either the sum squared error (SSE) or the cosine distance metric.

When the user clicks the run button, a non-targeted search, based on the user-defined parameters, is conducted to identify *m/z* values that will be considered for the SSN. The algorithm for the search is identical to the algorithm in the non-targeted tab of i2i.[10] Following, one of the *m/z* values is selected as an *anchor ion image* and the distance metric is calculated for all identified *m/z* values against the anchor ion image. To *normalize* the response of different ions, all compared *m/z* values are first scaled to the 99th percentile of intensity within their respective ion image. This allows for comparison across *m/z* values despite differences in absolute intensities. Subsequently, the anchor ion image is exchanged to ensure that all ion images of identified *m/z* values are compared with each other.

The equation used to calculate the SSN based on SSE and cosine distance is shown in Eq. 1 and Eq. 2, respectively. The x and y are intensities of the respective *m/z* in a given pixel, the x_{anchor} is the matrix of the anchor ion image and y_i is the matrix of the ion image for the *i*th ion.

$$SSE = \sum |x_{anchor} - y_i|^2 \qquad \textit{Eq. 1}$$

$$Cosine\ distance(x_{anchor}, y_i) = 1 - \frac{x_{anchor} \cdot y_i}{\|x_{anchor}\| \|y_i\|} \qquad \textit{Eq. 2}$$

The computational process creates a lower triangular correlation matrix with values corresponding to a similarity index (SI). The use of a lower triangular matrix saves memory usage and computation time during the search process. The ion images with high SI, as set by the user as the error limit, are grouped based on the user-selected percentile of the similarity index values to be included. For example, by selecting 0.1, only 10% of the lowest SI values (i.e. the SI values with the highest correlation) are used to generate a filtered correlation matrix. The error limit has to be optimized for each experiment with respect to the complexity of the given scan event. A graph in MATLAB is then created with the filtered correlation matrix, with each group in the correlation matrix corresponding to a connected component of the graph. Following, the function conncomp is used to extract the spatially correlated *m/z* values of the groups. The results are shown as clusters of *m/z* values with similar distributions, termed the SSN.

To interrogate the SSN, the user can select groups and their *m/z* values in the list box next to the displayed SSN. Alternatively, by opening the SSN as a plotted figure, the user can hover over the displayed SSN to view information on each node in real-time and save the plot. The number of individual SSN groups is ordered by size, with Group 1 being the largest. The graph layout, including the length of the lines within each SSN group, is automatically set by MATLAB and has no value for the interpretation of the SSN. For automatic annotation of the *m/z* values in the SSN based on user-selected ppm difference, the user can upload a database containing *m/z* values and known names of the corresponding ions. The annotated ions are identified in the list box by a green dot next to the *m/z* value. All SSN calculations and interrogation are supported by a GUI integrated into our i2i application (github: LanekoffLab),[10] and the functionalities are detailed in Extended Data Fig.

Immunostainings and tissue characterization

Fluorescent immunostainings were performed as previously published.[16] Briefly, frozen human tissue slides were dried at room temperature, fixed with 4% PFA at room temperature for 10 min, washed with PBS and incubated with blocking solution (10% normal species serum (NSS) in 0.05% Tween20 (Sigma-Aldrich)) for 30 min. Primary antibodies for PLP (1:300; Serotec, MCA839G), UEA-I (1:1000, Vector Labs B-1065), HLA-DR (1:500; Hybridoma) and Fibrinogen-FITC (1:300, Dako, F0111) were diluted in 1% NSS in 0.05% Tween20-PBS and applied on the slides overnight at 4 °C. Tissue sections were washed in PBS and incubated for 1 h with Alexa fluorophore-conjugated secondary antibody. Nuclear staining was performed using Hoechst fluorescent DNA stain (33258, Thermo Fisher Scientific) for 1 min. Images were acquired as a 20x overview scan at the Olympus VS200 slide scanner. Following, visual characterization was performed using QuPath software (version 0.4.4) to aid classification based on full (normal), diffuse (dirty appearing white matter) and absent (lesion) PLP immunoreactivity.[23]

Regions of interest selection and data extraction

Tissue samples from three non-neurological control (NNC) and five people with multiple sclerosis (PwMS) were analyzed using one brain tissue section for each subject. A multimodal approach was used to select ROIs unambiguously. In particular, a region had to fulfil two criteria to be considered as an ROI: i) have a morphologically

well-defined border from surrounding areas based on PLP and HLA-DR staining, ii) have a well-defined chemical profile based on ion images acquired using PA nano-DESI MSI. Morphologically distinct areas were defined according to the section "Immunostainings and tissue characterization" and stratified into normal, diffuse and absent PLP categories. (Extended Data Fig. 7). Chemically distinct areas were defined by segmenting the PA nano-DESI MSI ion images based on the spatial distribution of monoacylglycerol, phosphatidylcholine, phosphatidylethanolamine, prostaglandin, free fatty acid and sterol lipid classes. In total, 55 ROIs were identified: 19 normal PLP, 20 diffuse PLP, and 16 absent PLP (Supplementary Table 8).

To compare the abundance of cholesterol and oxidized cholesterol products, average pixel intensities were extracted from each ROI using the i2i software[10] and the fractional abundance (FA) was calculated (Eq 3). In Eq. 3, the FA is calculated for each oxysterol based on its intensity over the sum of intensities of cholesterol (ST1) and all selected oxysterols (ST3, ST4, ST7).

$$FA = \frac{Int_{oxysterol}}{\sum(Int_{oxysterols} + Int_{cholesterol})} \qquad \textit{Eq. 3}$$

Subsequently, the cholesterol oxidation level was defined according to Eq 4, where FA is the fractional abundance of the molecule, and ON is defined by the additional oxygens in the sum-composition formula compared to cholesterol (0 for ST1, 1 for ST2, 2 for ST3 and ST4, and 4 for ST7).

$$Oxidation\ level = \sum(FA_i \times ON_i) \qquad \textit{Eq. 4}$$

Statistical analysis

Statistical analysis was performed, and boxplots were created using R v4.3.2 in RStudio.[24] The normality of the data was tested using the Shapiro-Wilk test. The pilot study cohort was balanced for age and post-mortem delay, and the covariate significance of the distinct patient was tested using a Kruskal-Wallis test. Since it was significant in some cases and not significant in others, we decided to perform non-parametric one-way testing but denote each donor by color codes as per Supplementary Table 8. In multi-group comparisons, the Kruskal-Wallis test was performed, followed by Dunn´s post-test, where a significant difference was indicated. For the two-group comparisons, the Wilcoxon test was used. FDR correction was performed in all analyses using the Benjamini-Hochberg method. Significant differences are indicated in the plots as follows. *:p<0.05, **:p<0.01, ***:p<0.001, ****:p<0.0001. The results of statistical tests are detailed in Supplementary Table 10. In the boxplots, the black line denotes the median, the white dot the mean, the top and bottom edges of the box the interquartile range, and the whiskers extend to the minimum and maximum data points.

Hierarchical clustering-based heatmaps and Pearson correlation heatmaps and PLS-DA plots were created using MetaboAnalyst 6.0.[25] Missing data points were imputed by LOD (1/5 of the lowest intensity). For hierarchical clustering, values were Z-scored, Euclidean distance measure was set, and autoscaling was set based on samples.

References

21. Lanekoff, I. *et al.* Automated platform for high-resolution tissue imaging using nanospray desorption electrospray ionization mass spectrometry. *Anal Chem* **84**, 8351–8356 (2012).

22. Johan Lillja. Novel strategies to increase throughput and differentiate lipid isomers in mass spectrometry imaging. (Uppsala University, Uppsala, 2023).

23. Lassmann, H. Multiple Sclerosis Pathology. *Cold Spring Harb Perspect Med* **8**, a028936 (2018).

24. Ihaka, R. & Gentleman, R. R: A Language for Data Analysis and Graphics. *Journal of Computational and Graphical Statistics* **5**, 299 (1996).

25. Pang, Z. *et al.* MetaboAnalyst 6.0: towards a unified platform for metabolomics data processing, analysis and interpretation. *Nucleic Acids Res* **52**, W398–W406 (2024).

Data availability

Data has been uploaded to figshare

Code availability

The source code and the compiled version of the software will be made available upon acceptance of the manuscript at https://github.com/LanekoffLab

Acknowledgements

We thank the donors and their families for making the tissue available in the biobank and Dr. Johan Lillja for his contributions to the initial work and fruitful discussions.

Funding

Funding for this work was provided by the Swedish Research Council (2022-06628 and 2023-03384 to I.L.) and the European Union (ERC, 101041224 – X CELL to I.L.). Views and opinions expressed are, however, those of the author(s) only and do not necessarily reflect those of the European Union or the European Research Council. Neither the European Union nor the granting authority can be held responsible for them. This work was also supported by a grant from the Dutch Research Council (NWO Vidi grant 91719305 to G.K.).

Author contributions

I.L. conceived the study. R.M. developed the software. V.V.S and G.T. performed mass spectrometry imaging experiments, analyzed and visualized the data. G.K. provided samples, C.H. performed immunostaining experiments and G.T. and C.H. performed tissue classification. I.L., V.V.S., and G.T. wrote the original manuscript. All authors contributed to reviewing and correcting the manuscript and gave consent to the final version.

Competing interest

The authors declare no competing interests.

Extended data figures

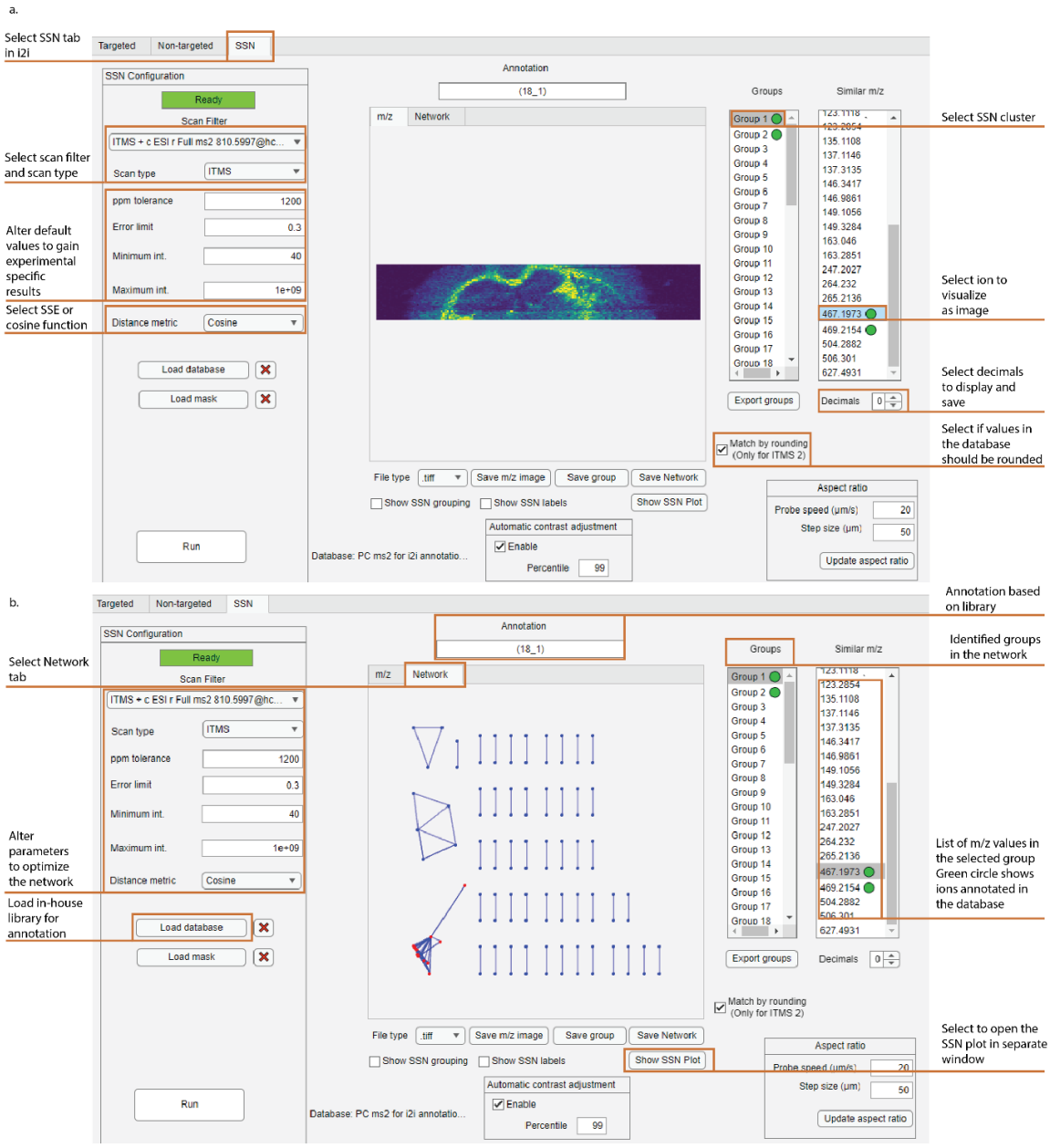

Extended Data Fig 1. GUI of the new SSN tab in i2i. The operator selects the scan filter and scan type based on the loaded data, along with the specified parameters. Default parameters are suggested, although optimization may be required for each scan filter depending on the complexity and intensity of the detected ions **(a)**. The SSN automatically clusters ions in the selected scan (here, FTMS, $FTMS^2$ or $ITMS^2$) into networks based on either the sum of squared error (SSE) or the cosine spatial similarity metric of the ion distributions. The network group and *m/z* of the ion image to be displayed are selected together with the relevant number of decimals or rounding, depending on the mass resolution. The product ion image in the *m/z* tab shows the acyl chain 18:0 (*m/z* 467.2 of $[PC(36:1)+Na]^+$ (*m/z* 810.2) with the annotated ions marked with a green dot. In the network tab, the resulting SSN is displayed **(b)**. The network shows nodes of *m/z* values that are clustered based on their spatial distributions. The number of individual SSN groups is ordered by size, with Group 1 being the largest. The graph layout, including the length of the lines within each SSN group, is automatically set by MATLAB and has no value for the interpretation of the SSN. To interrogate the SSN, the user can select groups and their *m/z* values in the list box next to the displayed SSN. Alternatively, by opening the SSN as a new window, the user can hover over the displayed SSN to view information on each node in real-time and save the plot. For the automatic annotation of m/z values in the SSN, based on ppm differences or rounding, the user can upload a database containing m/z values and the corresponding known names of the ions for matching (Supplementary Tables 1-4, 7). For experimental details, see Dataset 1 in Supplementary Table 9.

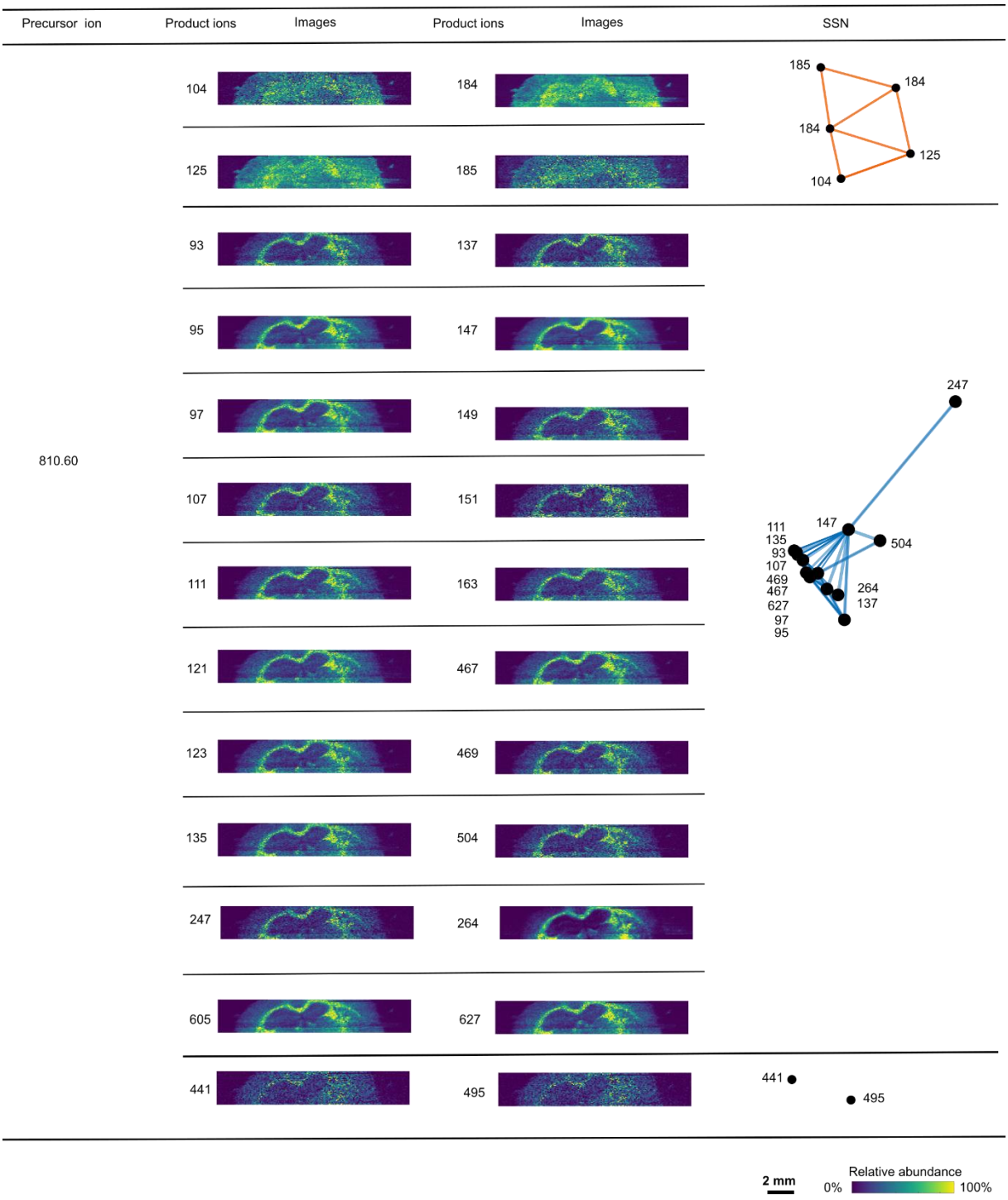

Extended Data Fig 2. Product ion image networks from PIA SSN. The *m/z* values and corresponding product ion images were acquired from the precursor window of 810.60 ± 0.35 Da using the PIA of a mouse brain tissue section. The subsequent SSN reveals that product ions are separated into two groups based on their spatial distribution, as shown by the orange and blue SSN, suggesting the presence of two structurally different precursors. Two additional disconnected nodes are present, indicating the presence of a third, but less abundant, precursor. From top to bottom, the represented ions are $[PC\ 38:4+H]^+$, $[PC\ 18:0_18:1+Na]^+$, and $[PC\ 16:0_20:1+Na]^+$. For experimental details see Dataset 1 in Supplementary Table 9.

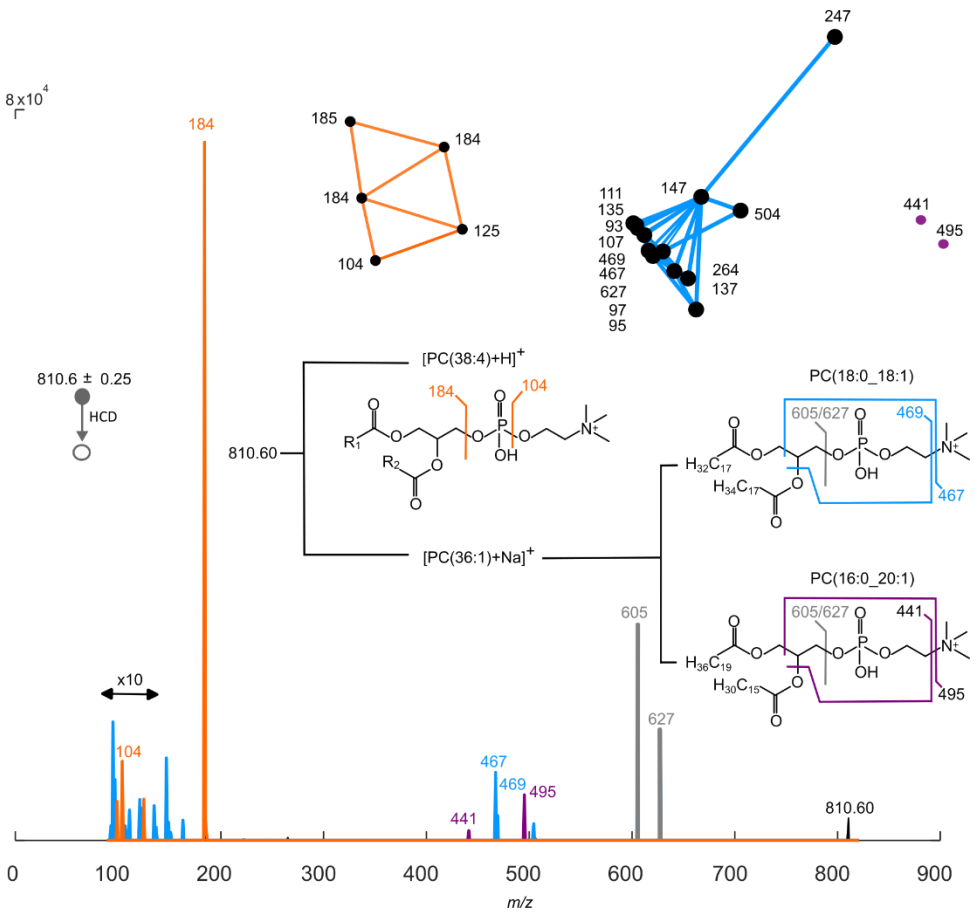

Extended Data Fig 3. **SSN deconvolutes product ion mass spectra and facilitates annotation of isobars and isomers.** The convoluted ITMS^2 mass spectrum produced from the product ions of all precursors in the 810.6 ± 0.35 window is readily deconvoluted by SSN. The product ions corresponding to the blue and orange SSN are shown in blue and orange, respectively. This shows that the two distinct isobars of [PC(38:4)+H]$^+$ and [PC(36:1)+Na]$^+$, which have different spatial distributions, both originate from the precursor ion at *m/z* 810.60. Furthermore, the data reveals that [PC(36:1)+Na]$^+$ consists of the two isomers PC(18:0_18:1) and PC(16:0_20:1). For experimental details see Dataset 1 in Supplementary Table 9.

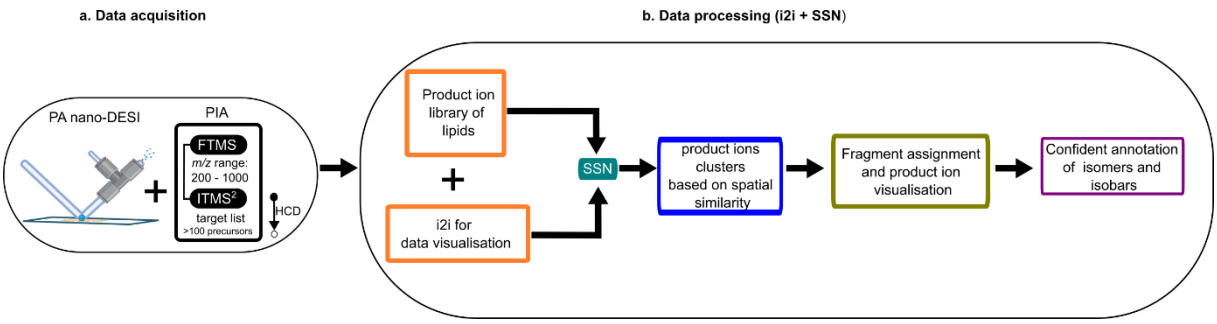

Extended Data Fig 4. Summary of PIA SSN workflow for imaging and metabolite annotation with PA nano-DESI. Tissue is placed on the PA nano-DESI platform and molecules are desorbed into the nano-DESI solvent liquid bridge between the two fused silica capillaries (50/150 µm i.d./o.d.). Ions generated from endogenous molecules through electrospray ionization are used to first fill the Orbitrap for a high-resolution FTMS full scan, which takes 1024 ms. Until the next FTMS scan event, the ion trap is filled for targeted $ITMS^2$ scan events after HCD. Depending on the ion abundance and, hence, the ion accumulation time, the number of $ITMS^2$ scans during the FTMS scan can vary. The complexity of the product ion scan will depend on the size of the precursor isolation window and the present isobars and isomers at the targeted *m/z* value. The SSN is performed for all pixels in the ion image based on the selected scan event, which can be performed in MS1 or MS^2 and with any mass analyzer. The SSN outputs a graphical view where each cluster of ions has a similar spatial distribution, and therefore stems from the same precursor ion. The product ions can be automatically annotated using an uploaded m/z database, and ion images from each cluster are readily interrogated in the “m/z” window to ensure distribution similarity. The ion distribution, therefore, serves as a third orthogonal parameter in conjunction with high mass resolution data and product ion spectra, ensuring high confidence in the annotation of ions, including isomers and isobars.

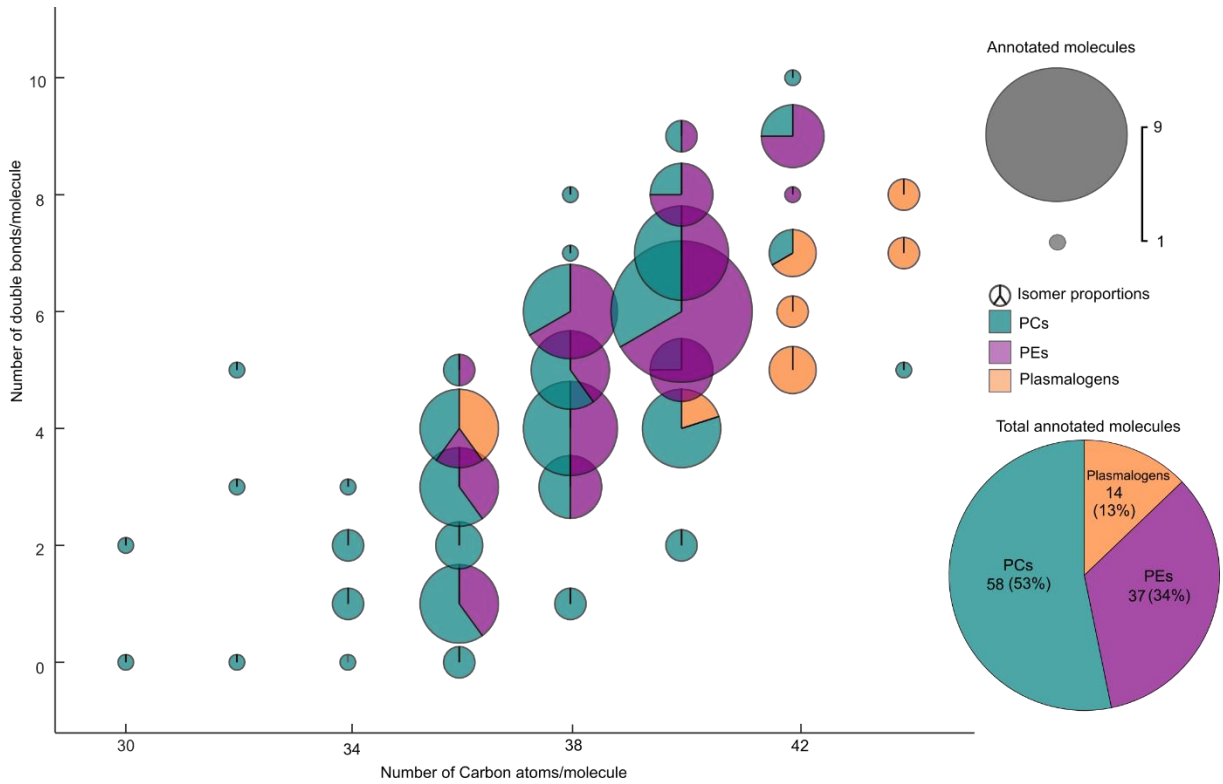

Extended Data Fig 5. **PIA SSN uncovers hidden isomers and isobars.** Total number of imaged and annotated PC, PE and PE-plasmalogen lipids in positive ion mode using PIA SSN on a mouse brain cross-sectional tissue section with 108 fragmentation windows of ± 0.35 Da. Of the 108 fragmentation windows, 34 were dedicated to phospholipids as sodiated adducts. In these mass channels, we annotated in total 134 phospholipid adducts with isobaric and isomeric precision. Out of these, 109 were unique phospholipid structures corresponding to 58 PCs, 37 PEs, and 14 PE plasmalogens. The color of the bubbles represents the respective lipid classes, and the size corresponds to the number of annotated species. For experimental details see Dataset 1 in Supplementary Table 9.

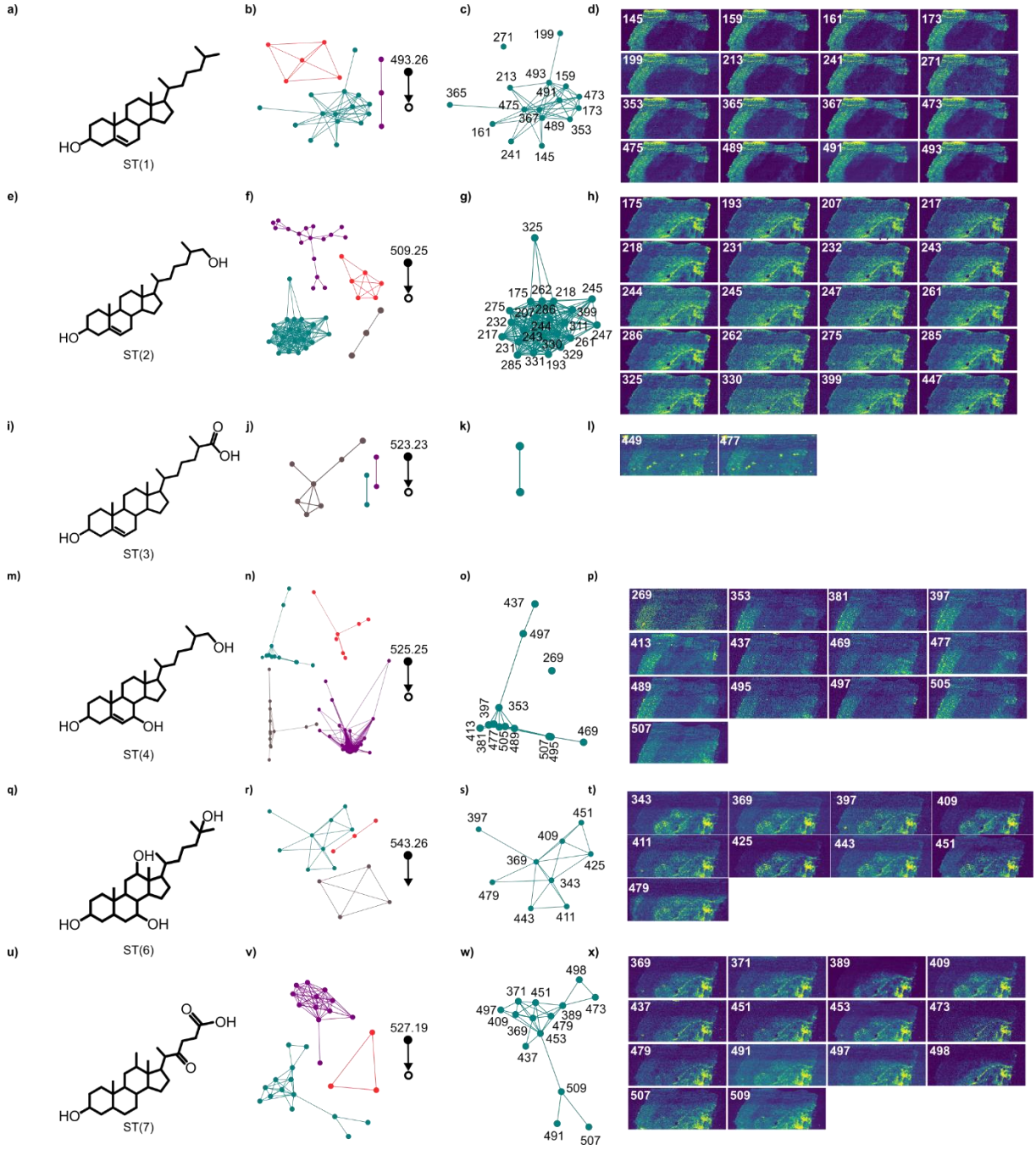

Extended Data Fig 6. The SSN deconvolutes complex ITMS^2 spectra produced by the fragmentation of co-isolated precursor ions. Characterization of oxysterol structures detected by PA nano-DESI MS^{2}I of human multiple sclerosis brain tissue. Structural annotation of cholesterol and oxidized cholesterol products using HCD of $[M+^{107}Ag]^+$ adduct in ITMS^2. **a-d** cholesterol, **e-h** hydroxycholesterol **i-l** hydroxycholestenoic acid, **m-p** dihydroxycholesterol, **q-t** cholestantetraol, **u-x** homodeoxycholic acid. For each targeted molecule, SSN and all product ions in the SSN are provided. One additional structural annotation (dihydroxy-cholestenoic acid) is shown in figure 2. For experimental details see Dataset 5 in Supplementary Table 9.

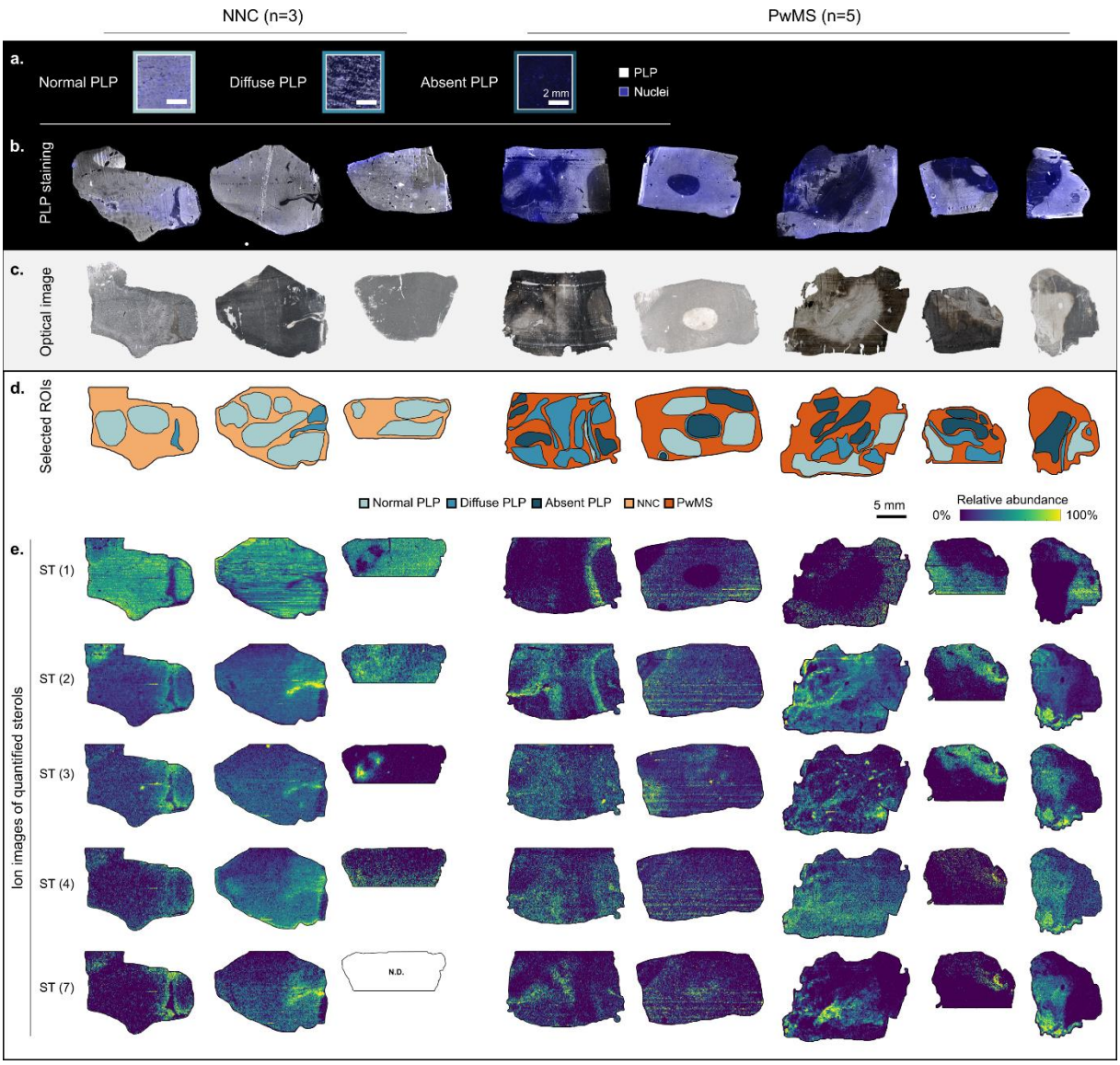

Extended Data Fig 7. Multimodal imaging of cholesterol and oxidized cholesterol products in human white matter brain tissue sections. Representative classifier images of fluorescent proteolipid protein (PLP) immunoreactivity were acquired as stated in the Methods section. Scalebar is 2 mm. **(a)** Full tissue scans of PLP immunoreactivity of human brain tissues (NNC=3, PwMS=5). Image intensities are scaled individually. **(b)** Brightfield microscopy images acquired using a Meyer Instruments PathScan Enabler IV slide scanner device. **(c)** Resulting ROIs for each tissue section, colored according to the PLP classification (light blue: normal PLP, medium blue: diffuse PLP, dark blue: absent PLP). **(d)** Ion images of cholesterol and oxidized cholesterol products in human white matter brain tissues from NNC and PwMS normalized to TIC and the 99th percentile intensity. Scalebar is 5 mm and applies to images **b-e**. N.D.: not detected. Subsequent tissue sections are used for PLP and MSI imaging modalities.

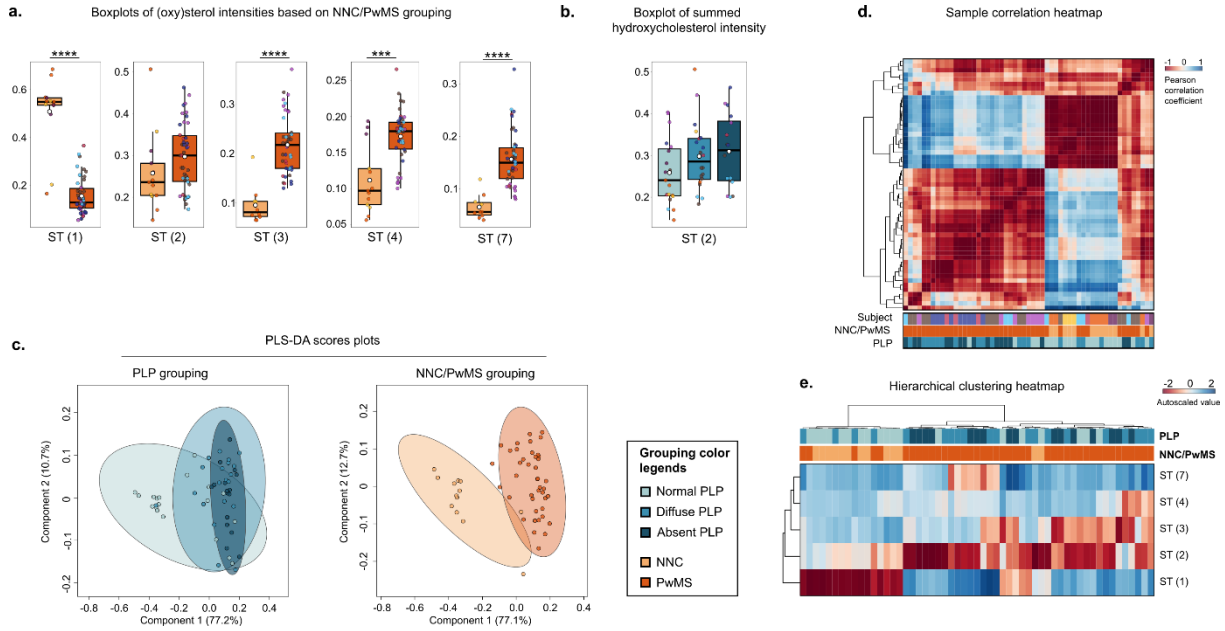

Extended Data Fig 8. Differentiation and clustering of brain tissue regions based on their oxysterol profiles. (a) Boxplots representing the fractional abundance of detected sterols between ROIs corresponding to NNC (light blue) and PwMS (orange) subject samples. Note that since quantitation is based on MS^1, the two detected isomers 24-hydroxycholesterol and 27-hydroxycholesterol are denoted together as ST(2). All other mass channels are confirmed by $FTMS^2I$ to only contain the annotated sterol. Significant differences were observed for all the molecules except ST(2). To define significance, Wilcoxon test with Benjamini-Hochberg FDR correction was performed (*:p<0.05, **:p<0.01, ***:p<0.001, ****:p<0.0001). Coloring of jitters displays data from individual subjects as denoted by Supplementary Table 8. **(b)** Boxplot representing the fractional abundance of ST(2) showing non-significant differences between ROIs corresponding to normal PLP (light blue), diffuse PLP (medium blue), and absent PLP (dark blue) subject samples. For additional boxplots, see Figure 2 in the main text. **(c)** PLS-DA analysis of sample grouping according to PLP and donor type (NNC vs PwMS) based on oxysterol profiling of ROIs. We observed only a slight differentiation of normal PLP ROIs from diffuse and absent PLP ROIs. However, a considerable differentiation is seen when the grouping is based on the subjects (NNC vs PwMS). This observation is further strengthened by the Pearson correlation heatmap of ROIs based on their (oxy)sterol profile **(d)** and the hierarchical clustering heatmap of (oxy)sterols across all ROIs **(e)**. For hierarchical clustering, Ward method with Euclidian distance measures was used and values were autoscaled within each ROI sample. The coloring of hues for the Pearson correlation coefficients and the autoscaled values for hierarchical clustering is displayed in the top right corner. We observed excellent clustering based on NNC/PwMS subject grouping. The dominant sterol in NNC samples was cholesterol (ST(1)), while for the PwMS samples, it was hydroxycholesterol (ST(2)). The latter, although not statistically significant, shows an increased abundance in PwMS. The differentiation is predominantly based on patient type, with a slight basis in the PLP abundance of each ROI. However, interpatient differences are considerably larger than those due to classification parameters. Therefore, a follow-up study with a larger sample size is required to draw further biological conclusions.